Aerospace Science and Technology 133 (2023) 108113

Contents lists available at ScienceDirect

Aerospace Science and Technology

journal homepage: www.elsevier.com/locate/aescte

Refined MagSail thrust model for preliminary mission design and trajectory optimization

Marco Bassetto [a,*], Nikolaos Perakis [b,c], Alessandro A. Quarta [a], Giovanni Mengali [a]

[a] Department of Civil and Industrial Engineering, University of Pisa, Italy
[b] Chair of Space Propulsion, Technical University of Munich, Germany
[c] Initiative for Interstellar Studies (i4is), United Kingdom

ARTICLE INFO

Article history:
Received 17 March 2022
Received in revised form 8 November 2022
Accepted 3 January 2023
Available online 10 January 2023
Communicated by Nikolaos Gatsonis

Keywords:
Magnetic sail
Thrust model
Trajectory optimization
Mission design

ABSTRACT

A magnetic sail is an advanced propellantless propulsion system concept for deep space missions, proposed by Dana Andrews and Robert Zubrin about 30 years ago. The thrust is generated by the electromagnetic interaction between the solar wind charged particles and an artificial magnetic field obtained through a large current-carrying coil made of superconducting material. This paper discusses an up-to-date single-loop magnetic sail thrust model based on the numerical and experimental results obtained in the last decade. In particular, a particle model is initially used to evaluate the performance of a reference configuration in terms of thrust components in a body reference frame. Then, some scaling relationships are used to estimate the magnetic sail performance as a function of the design parameters. The proposed thrust model is used to analyze the minimum-time transfer problem between two circular and coplanar heliocentric orbits. Minimum flight times necessary to complete ephemeris-free Earth-Venus and Earth-Mars transfers are calculated as a function of the magnetic sail characteristic size in a parametric way.

1. Introduction

The restricted amount of propellant, the need for gravity assist maneuvers [1], and the existence of narrow launch windows are the main limitations in the use of chemical thrusters for interplanetary missions [2,3]. Continuous-thrust propellantless propulsion systems represent an interesting alternative in case of high-energy transfers [4,5] or long-term missions in deep space [6–9]. In fact, these systems are able to exploit an external (that is, not stored on board) power source that guarantees a theoretically unlimited Δv capability. Among the propellantless thrusters, a number of scientific papers have been devoted to the study of solar sails [10–13], which exploit the solar irradiance, or to electric [14,15] and magnetic [16] sails, which exploit the electrically charged particles of the solar wind to generate thrust in the interplanetary space.

The idea of a magnetic sail (MagSail) was conceived at the end of the 80s by Andrews and Zubrin [16–20] as an advanced propulsion concept suitable for either interplanetary or interstellar scientific missions. A MagSail is a propellantless device consisting of a large current-carrying coil made of superconducting material. The electric current flowing in this coil generates an artificial magnetic field that interacts with the solar wind (SW) particles through the Lorentz force, thus giving rise to a thrust capable of maneuvering the spacecraft in deep space. The multi-coil MagSails have also been proposed in the recent literature [21], in which the magnetic field distribution is established by the superposition principle. In particular, according to Murayama et al. [21], the multi-coil MagSails could be used to create an ideal magnetic field structure. Fig. 1 shows an artistic illustration of a three-coil MagSail (courtesy of Steve Bowers).

Although the MagSail is usually described as a single- (or a multi-) coil, a MagSail-based spacecraft also includes the deployment system, a shielding structure necessary to protect the tethers and the sail from micrometeorites, and an additional power system [19]. Typically, the payload is placed at the center of the coil and is connected to it by a set of supporting tethers, which allow the spacecraft to displace its center of mass in the plane of the conducting coil [19]. The latter arrangement is used to perform the required attitude control, since the required control torque is obtained by creating a suitable displacement between the spacecraft center of mass and the center of pressure [19].

* Corresponding author.
E-mail addresses: marco.bassetto@ing.unipi.it (M. Bassetto), nikolaos.perakis@tum.de (N. Perakis), a.quarta@ing.unipi.it (A.A. Quarta), g.mengali@ing.unipi.it (G. Mengali).

https://doi.org/10.1016/j.ast.2023.108113
1270-9638/

Nomenclature

$\boldsymbol{a}$	propulsive acceleration vector, with $a = \|\boldsymbol{a}\|$. [mm/s^2]
$\{a_r, a_t, a_n\}$	components of $\boldsymbol{a}$ in $\mathcal{T}_{\text{RTN}}$ [mm/s^2]
$\hat{\boldsymbol{d}}$	auxiliary unit vector
$\boldsymbol{e}$	error vector
$\boldsymbol{f}$	dynamics vector
f	payload mass fraction
$\boldsymbol{F}$	thrust vector, [μN]
$\{F_r, F_t, F_n\}$	components of $\boldsymbol{F}$ in $\mathcal{T}_{\text{RTN}}$ [μN]
$\{F_x, F_y, F_z\}$	components of $\boldsymbol{F}$ in $\mathcal{T}_{\text{XYZ}}$ [μN]
H	Hamiltonian function
$\mathcal{H}$	maximized Hamiltonian
H_c	part of H that depends on the controls
I	electric current [A]
I_c	critical value of I [A]
$\{\hat{\boldsymbol{i}}, \hat{\boldsymbol{j}}, \hat{\boldsymbol{k}}\}$	unit vectors of $\mathcal{T}_{\text{XYZ}}$
J	cost function
j	electric current density [A/m^2]
$\boldsymbol{m}$	magnetic dipole moment [A m^2]
m_{tot}	total spacecraft mass [kg]
n_p	particle density [m^{-3}]
O	Sun's center of mass
R	conducting coil radius [m]
r	Sun-spacecraft distance [au]
$\{\hat{\boldsymbol{r}}, \hat{\boldsymbol{t}}, \hat{\boldsymbol{n}}\}$	unit vectors of $\mathcal{T}_{\text{RTN}}$
S	spacecraft center of mass
t	time [days]
$\mathcal{T}_{\odot}$	heliocentric polar reference frame
$\mathcal{T}_{\text{RTN}}$	radial-transverse-normal reference frame
$\mathcal{T}_{\text{XYZ}}$	body reference frame
$\boldsymbol{v}$	spacecraft velocity vector [km/s]
$\{v_r, v_t, v_n\}$	components of $\boldsymbol{v}$ in $\mathcal{T}_{\text{RTN}}$ [km/s]
v_{SW}	solar wind speed relative to S [km/s]
$\boldsymbol{x}$	state vector
α	incidence angle [rad]
α_d	angle between $\hat{\boldsymbol{d}}$ and $\hat{\boldsymbol{r}}$ [rad]
α_t	thrust angle [rad]
α_λ	primer vector angle [rad]
γ	flight path angle [rad]
δ	clock angle [rad]
δ_d	clock angle of $\hat{\boldsymbol{d}}$ [rad]
θ	pitch angle [rad]
$\boldsymbol{\lambda}$	costate vector
$\boldsymbol{\lambda}_p$	primer vector, with $\|\boldsymbol{\lambda}_p\| = \lambda_p$
$\{\lambda_r, \lambda_\varphi, \lambda_{v_r}, \lambda_{v_t}\}$	components of $\boldsymbol{\lambda}$
$\mu_\odot$	Sun's gravitational parameter [km^3/s^2]
ρ	mass density [kg/m^3]
τ	switching parameter
φ	spacecraft polar angle [rad]

Subscripts

0	initial
f	final

Subscripts

ref	reference
$\cdot$	time derivative
$\wedge$	unit vector
$\star$	optimal

List of acronyms

HTS	high-temperature superconducting
MDM	magnetic dipole moment
MHD	magnetohydrodynamic
IMF	interplanetary magnetic field
PIC	particle-in-cell
SiLM	single-loop MagSail
SW	solar wind

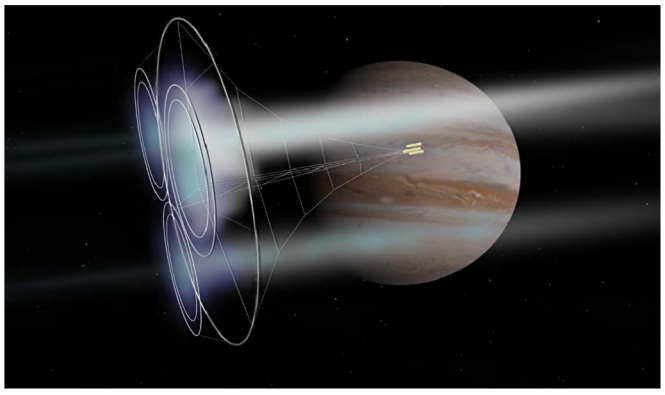

Fig. 1. Artistic illustration of a three-coil MagSail. Courtesy of Steve Bowers.

1.1. A short review of the recent studies on MagSail concept

In the last two decades, the results obtained from numerical simulations and experimental tests made on scale models have given important information about the MagSail performance. As far as numerical methods are concerned, the study of the interaction between the SW plasma particles and the magnetic field surrounding the MagSail has been addressed with different approaches. Fujita [22] analyzed the electromagnetic interaction between SW and moderately-sized MagSails when their size reduces to below the continuum limit at which the magnetohydrodynamic (MHD) approximations of the plasma flow fail. In his simulations, Fujita [22] used a hybrid particle-in-cell (PIC) method to take into account the finite Larmor-radius effect of the electromagnetic interaction between the plasma flow and the artificial magnetic field. By changing the size of the MagSail from several kilometers to a few thousand kilometers, Ref. [22] shows that the drag coefficient decreases as the ratio of the ion Larmor radius to the radius of the magneto-hydrodynamic interaction becomes greater than unity. Later, Akita and Suzuki [23] considered a 10 m MagSail to simulate the electromagnetic interaction between SW and a magnetic field using a full PIC method, while Nishida et al. [24,25] used the MHD model to deeply analyze how a variation in SW momentum is transferred to the spacecraft via the Lorentz force. More recently, a two-and-half-dimensional full PIC simulation was carried out by Moritaka et al. [26], who observed a magnetic inflation mediated by the gyration motion of the injected ions, which is responsible (when the artificial magnetosphere has a scale comparable with the gyration radius) for the formation of an ion-rich region near the direction-reversal position of the injected ions.

In the same years, Yamamoto et al. [27] performed three-dimensional ideal MHD simulations to show the effect of the interplanetary magnetic field (IMF) on the MagSail thrust. In particular, Yamamoto et al. [27] revealed that a high thrust is obtained when the IMF is perpendicular to the particle stream and to the magnetic dipole moment (MDM) generated by the superconducting coil, while Kajimura et al. [28] made three-dimensional hybrid (i.e.,

ion particle and electron fluid) PIC simulations in the range from the ion inertial scale to the MHD scale and showed that, independently of the magnetosphere size, the spacecraft attitude is stable when the MDM is perpendicular to the SW flow. Ashida et al. [29] evaluated the thrust characteristics of a MagSail by suggesting a new numerical model, including the ion finite Larmor-radius effect, in which the particle trajectories are solved based on a flux-tube model and the electrons are treated as a plasma fluid under the assumptions of quasi-neutrality and steady state conditions. The results found by Ashida et al. [29], which agree with those obtained by MHD and hybrid PIC models, were derived with a computational cost reduced by up to one tenth of that of the hybrid PIC model. Nishida and Funaki [30] used a resistive MHD model in a two-dimensional space and showed that, if the SW is not magnetized by the IMF, the sail attitude is stable when the MDM is perpendicular to the SW flow. Conversely, the IMF rotates the sail so as to align the MDM with the IMF, thus revealing that the sail stability is strongly affected by the IMF itself.

Using MHD and particle simulations, Funaki et al. [31] showed that the release of a low-velocity plasma from the MagSail excites an equatorial ring-current around the spacecraft, which creates a larger magnetosphere and a corresponding larger thrust magnitude. Nagasaki et al. [32] analyzed the current transport, the thermal characteristics, and the applied stresses of yttrium barium copper oxide (YBCO)-coated conductors for the optimal design of high-temperature superconducting (HTS) coils to be used in deep space as a propellantless propulsion system. Ashida et al. [33] performed three-dimensional PIC simulations on small-scale magnetospheres to investigate the thrust characteristics of small-scale MagSails. In particular, Ashida et al. [33] showed that the electron Larmor motion and the charge separation become significant, and the thrust is influenced by the cross-sectional area of the charge-separated plasma cavity. They also showed that the thrust generated by a small-scale MagSail is roughly proportional to the MDM, the SW density, and the SW speed. In another work, Ashida et al. [34] conducted two-dimensional PIC simulations on small-scale magnetospheres to investigate the thrust characteristics of a MagSail, assuming that the magnetosphere is inflated by an additional plasma injection. With this assumption, the authors [34] fund that the additional plasma injection can effectively increase the thrust by inducing a diamagnetic current in the same direction as the coil current. Finally, scaling laws using particle simulations were derived by Gros [35] for the MagSail axial configuration.

In the field of experimental investigations of small-scale MagSails, Kojima et al. [36] conducted a scaled-down laboratory experiment in a space chamber and showed the feasibility of a MagSail simulator, although in the absence of a collision-less SW plasma flow, while Funaki et al. [37–39] designed a laboratory simulator in a space chamber with a diameter of 2 m, in which a high-power magnetoplasmadynamic arcjet was operated to provide a high-speed hydrogen plasma plume. Later, Ueno et al. [40] used a magnetoplasmadynamic arcjet to produce a plasma flow simulating the SW and conducted direct thrust measurements by a parallelogram-pendulum method. Kajimura et al. [41] used laboratory experiments to check the agreement between the results from three-dimensional hybrid PIC simulations and those from experimental tests, when the simulations are carried out by considering the ion-neutral collision effect. By simulating the SW with a plasma jet, Oshio et al. [42] found that the thrust level changes quickly in response to SW fluctuations. Nagasaki et al. [43] fabricated a double-pancake coil using a Bi-2223/Ag tape with a length of 200 m as a scale-down model for a MagSail and measured the current transport property and temperature rise during current applications of the HTS coil in a conduction-cooled system. Finally, Murayama et al. [21] developed a multi-coil MagSail consisting of three small conducting coils in order to improve its efficiency in capturing the SW.

1.2. MagSail-based mission scenarios and the contribution of this work

Several potential mission scenarios exist in which a MagSail-based spacecraft might be usefully employed. For example, Shah [44] suggested to use a MagSail to perform transfers from the Earth to the Moon, while Love and Andrews [45] proposed to use a MagSail for the inspection of an asteroid, for the orbital correction of spacecraft in unstable libration points or near planets with magnetic fields, and for aerobraking purposes in planetary ionospheres. In addition, Andrews [46] identified the MagSail as a near-term technology suitable for interstellar travels.

About ten years ago, collecting the results from the theoretical analyses conducted by Zubrin and Andrews [19], the numerical simulations carried out by Kajimura et al. [28], and the experimental tests performed by Nishida and Funaki [30], Quarta et al. [47] proposed a simple MagSail thrust model, which was employed to investigate minimum-time orbital transfers and locally optimal escape trajectories from the Solar System. The same thrust model was recently used to analyze displaced non-Keplerian orbits around the Sun [48] and tight spiral trajectories through an analytical (approximate) approach [49]. Finally, Perakis and Hein [50] suggested to combine a MagSail (which is more effective at high inertial velocities) and an electric solar wind sail [51–53] (which has better performance at low speeds) for interstellar deceleration, while Perakis [54] showed that a change in the orbital inclination can be achieved with a single-coil MagSail through a bang-bang control of the pitch angle.

The aim of this study is to update the thrust model developed by Quarta et al. [47] by means of the results obtained in the last decade. More precisely, this paper presents an up-to-date thrust model for a **Si**ngle-**L**oop **M**agSail (SiLM) and exploits it in the analysis of minimum-time heliocentric transfer trajectories. In particular, the new SiLM thrust model is used to study the time-optimal transfer between two circular and coplanar heliocentric orbits [55,56]. To that end, the optimal control law for a SiLM is first determined numerically, then, circle-to-circle Earth-Venus and Earth-Mars transfers for a MagSail-based spacecraft are analyzed using an indirect method [57–59]. Using a simplified spacecraft mass breakdown model, the minimum flight times are estimated, for a given value of the payload mass fraction, as a function of the coil radius, to which the propulsive acceleration is directly proportional.

The remainder of the paper is organized as follows. Section 2 models the SiLM performance with a particle method and analyzes the thrust as a function of the Sun-spacecraft distance, the superconducting coil radius, the electric current, and the SW speed relative to the spacecraft. Section 3 derives the thrust vector components in a radial-transverse-normal reference frame, while the propulsive acceleration vector (related to the thrust through the total mass of the spacecraft) is calculated in Section 4. The optimal control law is analyzed in Section 5, where the necessary conditions for optimality according to the Pontryagin's maximum principle are illustrated in the case of a circle-to-circle transfer. Section 6 evaluates, as a function of the coil radius, the minimum flight time in two typical interplanetary transfers. Finally, the last section contains the concluding remarks.

2. MagSail performance evaluation through particle method

This section analyzes the propulsive performance of a reference SiLM configuration (superscript ref) using a particle method. The details of the reference SiLM used in the numerical simulations

Table 1
Reference SiLM configuration used in the numerical simulations.

Parameter	Value
R^{ref}	100 m
I^{ref}	10^5 A
n_p^{ref}	2×10^7 m^{-3}
$v_{\text{SW}}^{\text{ref}}$	5×10^5 m/s

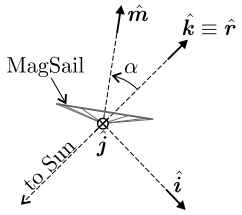

Fig. 2. Sketch of $\mathcal{T}_{\text{XYZ}}$ reference frame, where the unit vector $\hat{\boldsymbol{j}}$ enters the sheet.

are reported in Table 1, where the parameters $\{R,\, I,\, n_p,\, v_{\text{SW}}\}$ represent the (single) coil radius, electric current, particle density, and SW speed relative to the spacecraft, respectively. Note that n_p^{ref} refers to the reference distance from the Sun $r^{\text{ref}} \triangleq 0.5$ au.

The thrust vector components of the reference SiLM are obtained in an orbital reference frame $\mathcal{T}_{\text{XYZ}}(S;\, \hat{\boldsymbol{i}},\, \hat{\boldsymbol{j}},\, \hat{\boldsymbol{k}})$, with its origin at the spacecraft center of mass S and unit vectors $\{\hat{\boldsymbol{i}},\, \hat{\boldsymbol{j}},\, \hat{\boldsymbol{k}}\}$; see Fig. 2. The latter are related to the radial (i.e., Sun-spacecraft) unit vector $\hat{\boldsymbol{r}}$ and to the MDM vector $\boldsymbol{m}$ as

$$\hat{\boldsymbol{i}} \triangleq \frac{\cos\alpha\, \hat{\boldsymbol{r}} - \hat{\boldsymbol{m}}}{\sin\alpha} \quad , \quad \hat{\boldsymbol{j}} \triangleq \frac{\hat{\boldsymbol{m}} \times \hat{\boldsymbol{r}}}{\sin\alpha} \quad , \quad \hat{\boldsymbol{k}} \triangleq \hat{\boldsymbol{r}} \tag{1}$$

where $\hat{\boldsymbol{m}} \triangleq \boldsymbol{m}/\|\boldsymbol{m}\|$, and $\alpha \in [0,\, \pi]$ rad is the incidence angle, defined as the angle between the directions of $\hat{\boldsymbol{m}}$ and $\hat{\boldsymbol{r}}$, viz.

$$\alpha \triangleq \arccos\left(\hat{\boldsymbol{m}} \cdot \hat{\boldsymbol{r}}\right) \tag{2}$$

Note that the unit vectors $\{\hat{\boldsymbol{i}},\, \hat{\boldsymbol{j}}\}$ are not defined when $\sin\alpha = 0$, that is, when the direction of $\hat{\boldsymbol{m}}$ is parallel to that of $\hat{\boldsymbol{r}}$.

Fig. 3 summarizes the results of the numerical simulations obtained with the reference SiLM and, in particular, how the thrust components

$$F_x^{\text{ref}} \triangleq \boldsymbol{F}^{\text{ref}} \cdot \hat{\boldsymbol{i}} \quad , \quad F_y^{\text{ref}} \triangleq \boldsymbol{F}^{\text{ref}} \cdot \hat{\boldsymbol{j}} \quad , \quad F_z^{\text{ref}} \triangleq \boldsymbol{F}^{\text{ref}} \cdot \hat{\boldsymbol{k}} \tag{3}$$

change with α, where $\boldsymbol{F}^{\text{ref}}$ is the thrust vector of the reference SiLM. Note that the (discrete) data of the numerical simulations relating to each thrust component have been connected with a polygonal chain to facilitate the understanding of the figure itself.

Starting from the simulation results relative to the reference SiLM, it is useful to investigate how the thrust components $\{F_x,\, F_y,\, F_z\}$ scale with the particle density n_p (or the Sun-spacecraft distance r), the coil radius R, the electric current I, and the SW speed v_{SW}. Since the thrust magnitude F is proportional to n_p (and n_p is inversely proportional to r^2), it turns out that

$$F \propto \left(\frac{r^{\text{ref}}}{r}\right)^2 \tag{4}$$

In addition, the thrust magnitude is directly proportional to the sail area, therefore

$$F \propto \left(\frac{R}{R^{\text{ref}}}\right)^2 \tag{5}$$

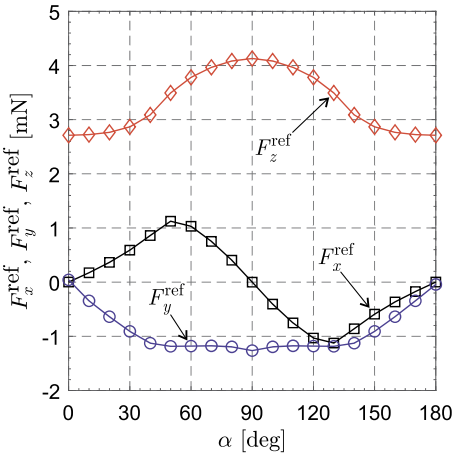

Fig. 3. Thrust components in the reference SiLM.

More complex is the variation of F with I and v_{SW}, which can be modeled using the following expression

$$F \propto \left[\frac{\ln\left(\dfrac{c\, I}{v_{\text{SW}}\, I_c}\right)}{\ln\left(\dfrac{c\, I^{\text{ref}}}{v_{\text{SW}}^{\text{ref}}\, I_c}\right)}\right]^n \tag{6}$$

where c is the speed of light, $I_c \triangleq 1.303 \times 10^6$ A is a critical current [35], and $n \triangleq 3.347$. Note that the thrust magnitude increases with I and decreases with v_{SW}. The latter behavior is explained by the fact that, due to their higher speed, the solar wind particles spend less time in the presence of a sufficiently strong magnetic field and, as such, they interact with it minimally [54]. Using Eqs. (4)–(6), the following variation of the thrust vector with $\{r,\, R,\, I,\, v_{\text{SW}}\}$ is obtained

$$\boldsymbol{F} = \boldsymbol{F}^{\text{ref}} \left(\frac{r^{\text{ref}}}{r}\right)^2 \left(\frac{R}{R^{\text{ref}}}\right)^2 \left[\frac{\ln\left(\dfrac{c\, I}{v_{\text{SW}}\, I_c}\right)}{\ln\left(\dfrac{c\, I^{\text{ref}}}{v_{\text{SW}}^{\text{ref}}\, I_c}\right)}\right]^n \tag{7}$$

3. Thrust vector components in $\mathcal{T}_{\text{RTN}}$

Starting from the previous numerical results, this section describes the thrust vector components in a radial-transverse-normal reference frame $\mathcal{T}_{\text{RTN}}(S;\, \hat{\boldsymbol{r}},\, \hat{\boldsymbol{t}},\, \hat{\boldsymbol{n}})$ of origin S, where the unit vectors $\{\hat{\boldsymbol{r}},\, \hat{\boldsymbol{t}},\, \hat{\boldsymbol{n}}\}$ are defined through the inertial spacecraft position $\boldsymbol{r}$ and the velocity vector $\boldsymbol{v}$ as

$$\hat{\boldsymbol{r}} \triangleq \frac{\boldsymbol{r}}{r} \quad , \quad \hat{\boldsymbol{t}} \triangleq \frac{\hat{\boldsymbol{v}} - \sin\gamma\, \hat{\boldsymbol{r}}}{\cos\gamma} \quad , \quad \hat{\boldsymbol{n}} \triangleq \hat{\boldsymbol{r}} \times \hat{\boldsymbol{t}} \equiv \frac{\hat{\boldsymbol{r}} \times \hat{\boldsymbol{v}}}{\cos\gamma} \tag{8}$$

where $r \triangleq \|\boldsymbol{r}\|$ is the Sun-spacecraft distance, $\hat{\boldsymbol{v}} \triangleq \boldsymbol{v}/\|\boldsymbol{v}\|$ is the velocity direction, and $\gamma \in [-\pi/2,\, \pi/2]$ rad is the flight path angle, that is, the angle between $\boldsymbol{v}$ and the local horizontal plane, viz.

$$\gamma \triangleq \arctan\left(\frac{\hat{\boldsymbol{r}} \cdot \hat{\boldsymbol{v}}}{\left\|\hat{\boldsymbol{r}} \times \hat{\boldsymbol{v}}\right\|}\right) \tag{9}$$

In order to express the components of $\boldsymbol{F}$ in $\mathcal{T}_{\text{RTN}}$ as a function of $\{F_x,\, F_y,\, F_z\}$, it is necessary to introduce a new angle, here referred to as "clock angle" and indicated with $\delta \in [0,\, 2\pi)$ rad, which represents the angle between the projection of $\hat{\boldsymbol{m}}$ on the local horizontal plane and the transverse unit vector $\hat{\boldsymbol{t}}$, that is

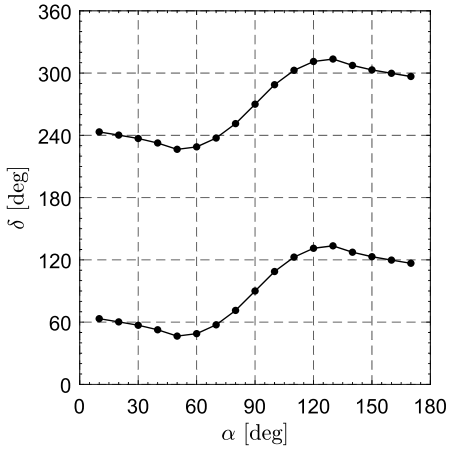

Fig. 4. Clock angle δ as a function of α when $F_n = 0$.

$$\sin\delta \triangleq \frac{\hat{\boldsymbol{m}}\cdot\hat{\boldsymbol{n}}}{\sin\alpha} \quad , \quad \cos\delta \triangleq \frac{\hat{\boldsymbol{m}}\cdot\hat{\boldsymbol{t}}}{\sin\alpha} \tag{10}$$

The rotation matrix $\mathbb{T}_{\mathrm{XYZ}\to\mathrm{RTN}}$ from $\mathcal{T}_{\mathrm{XYZ}}$ to $\mathcal{T}_{\mathrm{RTN}}$ is given by

$$\mathbb{T}_{\mathrm{XYZ}\to\mathrm{RTN}} = \begin{bmatrix} 0 & 0 & 1 \\ -\cos\delta & \sin\delta & 0 \\ -\sin\delta & -\cos\delta & 0 \end{bmatrix} \tag{11}$$

and the components $\{F_r, F_t, F_n\}$ of the thrust vector $\boldsymbol{F}$ in $\mathcal{T}_{\mathrm{RTN}}$, defined as

$$F_r \triangleq \boldsymbol{F}\cdot\hat{\boldsymbol{r}} \quad , \quad F_t \triangleq \boldsymbol{F}\cdot\hat{\boldsymbol{t}} \quad , \quad F_n \triangleq \boldsymbol{F}\cdot\hat{\boldsymbol{n}} \tag{12}$$

are given by

$$F_r = F_z \tag{13}$$

$$F_t = -F_x\cos\delta + F_y\sin\delta \tag{14}$$

$$F_n = -F_x\sin\delta - F_y\cos\delta \tag{15}$$

3.1. Two-dimensional transfers

In case of a two-dimensional transfer, the normal component of the thrust is equal to zero, that is, $F_n = 0$. This situation constrains the value of δ, which now takes only two values corresponding to angles differing by 180 deg, that is

$$\delta = \mathrm{atan2}\left(\mp F_y, \pm F_z\right) \tag{16}$$

and δ depends on α as reported in Fig. 4.

In this case let $\alpha_t \in [-\pi/2, \pi/2]$ rad be the thrust angle, that is, the angle between the thrust vector and the radial direction, defined as

$$\alpha_t = \arctan\left(\frac{F_t}{F_r}\right) \tag{17}$$

which is positive (or negative) when $\boldsymbol{F}\cdot\boldsymbol{v} > 0$ (or $\boldsymbol{F}\cdot\boldsymbol{v} < 0$). Note that the special situation when $F_t = 0$ corresponds to a purely radial thrust. The thrust magnitude $F \equiv \sqrt{F_r^2 + F_t^2}$ and the thrust angle α_t of the reference SiLM are plotted, as a function of α, in Fig. 5 when $F_n = 0$. Each value of α corresponds to a single value of F and to two opposite values of α_t, and Fig. 5 shows that the reference SiLM can generate a maximum (or minimum) thrust angle of about 25 deg (or -25 deg).

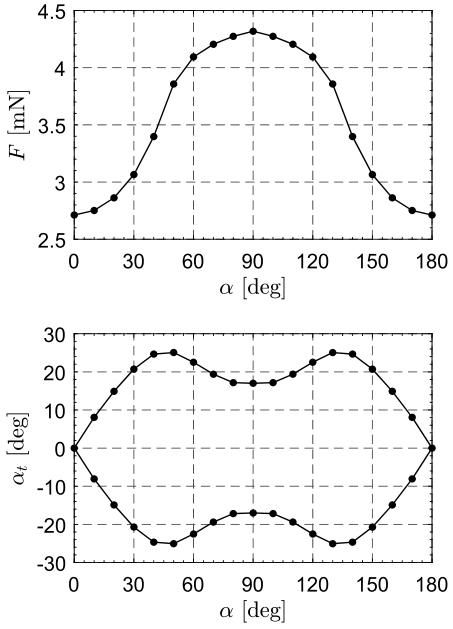

Fig. 5. Reference SiLM: thrust magnitude F and thrust angle α_t as a function of α when $F_n = 0$.

4. Propulsive acceleration vector

This section provides the expression of the propulsive acceleration vector $\boldsymbol{a}$, equal to the ratio of the thrust vector $\boldsymbol{F}$ to the total spacecraft mass m_{tot}, the latter being estimated with a suitable mass breakdown model. Following Ref. [60], the mass of the SiLM is related to the (single) coil mass m_{coil} as

$$m_{\mathrm{sail}} = 3.75\, m_{\mathrm{coil}} \tag{18}$$

where, according to Zubrin and Andrews [19], m_{coil} depends on the sail radius R, the coil mass density ρ, the electric current I, and the current density j as

$$m_{\mathrm{coil}} = 2\pi\, R\, \rho\, I/j \tag{19}$$

Taking Eqs. (18) and (19) into account, the total spacecraft mass is then given by

$$m_{\mathrm{tot}} = m_{\mathrm{pay}} + 3.75\, m_{\mathrm{coil}} \equiv m_{\mathrm{pay}} + k\, R\, I \tag{20}$$

where m_{pay} is the payload mass, while $k \triangleq 7.5\pi\,\rho/j$ is approximately equal to 1.5×10^{-5} kg/m/A assuming that $\rho = 6315$ kg/m^3 (the density of copper(II) oxide [54]) and $j = 10^{10}$ A/m^2 [61,62]. An equivalent expression of the payload mass is written in the form

$$m_{\mathrm{pay}} = f\, m_{\mathrm{tot}} \tag{21}$$

where $f \in (0, 1)$ is the dimensionless fraction of the total mass. Substituting Eq. (21) into Eq. (20), the total spacecraft mass is given by

$$m_{\mathrm{tot}} = \frac{k\, R\, I}{1 - f} \tag{22}$$

Bearing in mind Eq. (7), the following relationship of proportionality between the propulsive acceleration magnitude $a \triangleq \|\boldsymbol{a}\|$ and $\{r,\ R,\ I,\ v_{\mathrm{SW}},\ f\}$ holds

$$a \propto \frac{R\left[\ln\left(\dfrac{c\, I}{v_{\mathrm{SW}}\, I_c}\right)\right]^n (1-f)}{r^2\, I} \tag{23}$$

In other terms, the propulsive acceleration magnitude turns out to be directly proportional to R and inversely proportional to r^2, to decrease linearly with f, and to decrease with v_{SW}. Recall that v_{SW} is affected not only by the SW fluctuations, but also by the spacecraft radial velocity. As far as the dependence of a on I is concerned, the propulsive acceleration magnitude is maximized with respect to I by maximizing the function $\left[\ln\left(\frac{c\,I}{v_{SW}\,I_c}\right)\right]^n / I$, that is, when

$$I = \mathcal{I} \triangleq \frac{\exp(n)\, v_{SW}\, I_c}{c} \tag{24}$$

which is approximately equal to 6×10^4 A when $v_{SW} \equiv v_{SW}^{ref}$. Note also that $\mathcal{I}$ is directly proportional to v_{SW}.

The propulsive acceleration vector is given by

$$\boldsymbol{a} = \frac{\tau\ (1-f)}{k\,R\,I}\left(\frac{r^{ref}}{r}\right)^2\left(\frac{R}{R^{ref}}\right)^2\left[\frac{\ln\left(\frac{c\,I}{v_{SW}\,I_c}\right)}{\ln\left(\frac{c\,I^{ref}}{v_{SW}^{ref}\,I_c}\right)}\right]^n \boldsymbol{F}^{ref} \tag{25}$$

where the switching parameter $\tau \in \{0,\ 1\}$ is here introduced to account for possible coasting phases (case of $\tau = 0$) in the spacecraft trajectory. The components of $\boldsymbol{a}$ in $\mathcal{T}_{RTN}$ are

$$a_r \triangleq \boldsymbol{a}\cdot\hat{\boldsymbol{r}} \quad , \quad a_t \triangleq \boldsymbol{a}\cdot\hat{\boldsymbol{t}} \quad , \quad a_n \triangleq \boldsymbol{a}\cdot\hat{\boldsymbol{n}} \tag{26}$$

Neglecting the SW fluctuations and observing that, usually, $\left|\boldsymbol{v}\cdot\hat{\boldsymbol{r}}\right| \ll v_{SW}$, it is reasonable to assume that $v_{SW} \simeq v_{SW}^{ref}$. Moreover, by setting $I = \mathcal{I}$, Eq. (25) becomes

$$\boldsymbol{a} = \frac{\tau\, K\, R\ (1-f)}{r^2}\,\boldsymbol{F}^{ref} \tag{27}$$

where $K \simeq 3.9 \times 10^{17}$ m/kg. In summary, Eq. (27) represents the propulsive acceleration vector of a SiLM-based spacecraft when $\rho = 6315$ kg/m^3, $j = 10^{10}$ A/m^2, $v_{SW} \simeq v_{SW}^{ref}$, and $I = \mathcal{I}$. In this case, the design parameters reduce to R and f only. Note that, by suitably increasing the sail radius R, it is possible to increase the payload mass fraction f while keeping the propulsive acceleration fixed. Of course, this leads to an increase in the total spacecraft mass m_{tot}.

5. Optimal control law and trajectory optimization

For given values of R and f, the first step in the search for minimum-time trajectories is the evaluation of the triplet $\{\alpha^\star,\ \delta^\star,\ \tau^\star\}$ that maximizes the projection of the propulsive acceleration vector $\boldsymbol{a}$ along a prescribed direction. In this preliminary study, we assume that the SiLM performs a minimum-time transfer between two (heliocentric) circular coplanar orbits.

In this case, the value of $\delta^\star$ is constrained by Eq. (16) and, accordingly, $\{\alpha_t^\star, \tau^\star\}$ become the controls to be found in an optimal manner [63]. When dealing with coplanar transfers, a generic direction may be described by a two-dimensional unit vector $\hat{\boldsymbol{d}}$, defined as

$$\hat{\boldsymbol{d}} \triangleq \cos\alpha_d\,\hat{\boldsymbol{r}} + \sin\alpha_d\,\hat{\boldsymbol{t}} \tag{28}$$

where $\alpha_d \in [-\pi,\ \pi]$ rad is the angle between $\hat{\boldsymbol{d}}$ and $\hat{\boldsymbol{r}}$; see Fig. 6. Note that $\alpha_d \geq 0$ if $\hat{\boldsymbol{d}}\cdot\hat{\boldsymbol{t}} \geq 0$, while $\alpha_d < 0$ if $\hat{\boldsymbol{d}}\cdot\hat{\boldsymbol{t}} < 0$.

The problem of maximizing the projection of $\boldsymbol{a}$ along $\hat{\boldsymbol{d}}$ amounts to maximizing the scalar product between $\boldsymbol{a}$ and $\hat{\boldsymbol{d}}$. To that end, consider the cost function $J = J(\alpha_t,\ \tau)$, defined as

$$J \triangleq \boldsymbol{a}\cdot\hat{\boldsymbol{d}} = a_r\,\cos\alpha_d + a_t\,\sin\alpha_d \tag{29}$$

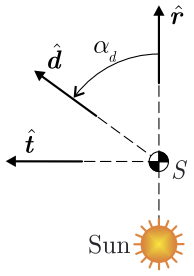

Fig. 6. Sketch of unit vector $\hat{\boldsymbol{d}}$.

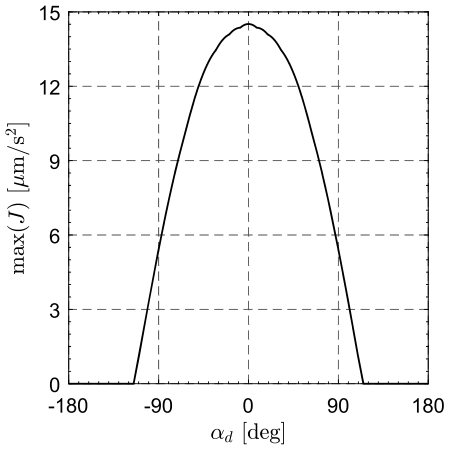

Fig. 7. Variation of $\max(J)$ with α_d when $f = 0.5$.

The maximum of J is shown in Fig. 7 as a function of α_d, for the reference SiLM, when $f = 0.5$. Note that the graph shown in Fig. 7 is smooth because J depends on the (continuous) variable α_d (see Eq. (29)) and no interpolation is performed. According to Eqs. (18)–(20), $m_{tot} \simeq 298$ kg. In particular, the fact that $\max(J) = 0$ when $|\alpha_d| > 115$ deg means that, in those cases, the projection of $\boldsymbol{a}$ along $\hat{\boldsymbol{d}}$ is maximized by switching the SiLM off, that is, by setting $\tau = 0$. The optimal control parameters $\alpha_t^\star$ and $\tau^\star$ are shown in Fig. 8 as a function of α_d. Note that the step-wise nature of the curve is due to the use of discrete data taken from the simulations, which have not been interpolated. Of course, the curve can be made smoother by setting a larger number of discrete points. However, a not too refined thrust model is already adequate for preliminary mission analysis purposes, that is, to estimate the flight times required to perform an orbital transfer as a function of the conducting coil radius.

A heliocentric polar reference frame $\mathcal{T}_\odot(O;\ r,\ \varphi)$ is now introduced, whose origin O coincides with the center of mass of the Sun (with gravitational parameter $\mu_\odot$) and φ is the polar angle measured from the Sun-spacecraft line at the initial time $t = t_0 \triangleq 0$; see Fig. 9. The SiLM trajectory is analyzed in an optimal framework by minimizing the flight time t_f required to transfer the spacecraft from a circular parking orbit of radius r_0 to a coplanar target orbit of given radius $r_f \neq r_0$. The optimization problem consists in finding the optimal controls $\alpha_t = \alpha_t^\star(t)$ and $\tau = \tau^\star(t)$ that maximize the performance index

$$\mathcal{J} \triangleq -t_f \tag{30}$$

subject to the nonlinear dynamics

$$\begin{cases} \dot{\boldsymbol{x}}(t) = \boldsymbol{f}\left(\boldsymbol{x}(t),\ \alpha_t(t),\ \tau(t)\right) \\ \boldsymbol{x}(0) = \boldsymbol{x}_0 \\ \boldsymbol{e}(\boldsymbol{x}(t_f)) = \boldsymbol{0} \end{cases} \tag{31}$$

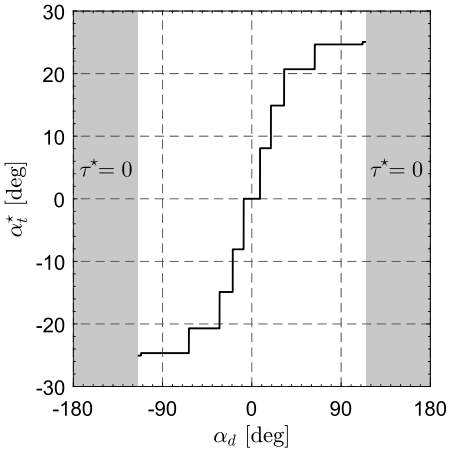

Fig. 8. Optimal controls $\alpha_t^\star$ and $\tau^\star$ as a function of α_d.

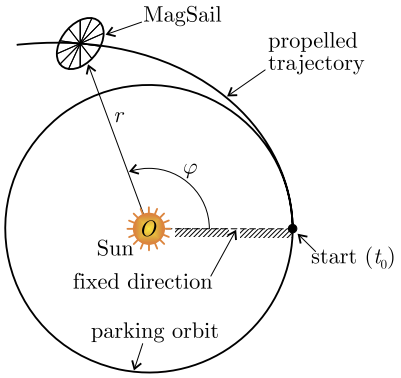

Fig. 9. Sketch of the heliocentric polar reference frame.

where

$$\boldsymbol{x} \triangleq [r \quad \varphi \quad v_r \quad v_t]^{\mathrm{T}} \tag{32}$$

is the state vector, $v_r \triangleq \boldsymbol{v} \cdot \hat{\boldsymbol{r}}$ is the radial component of the spacecraft velocity and $v_t \triangleq \boldsymbol{v} \cdot \hat{\boldsymbol{t}}$ is the transversal component of the spacecraft velocity, while

$$\boldsymbol{x}_0 \triangleq \begin{bmatrix} r_0 \\ 0 \\ 0 \\ \sqrt{\mu_\odot / r_0} \end{bmatrix} \quad , \quad \boldsymbol{e}(\boldsymbol{x}(t_f)) \triangleq \begin{bmatrix} r(t_f) - r_f \\ v_r(t_f) \\ v_t(t_f) - \sqrt{\mu_\odot / r_f} \end{bmatrix} \tag{33}$$

are the state vector at the initial time and the error vector at the (unknown) final time t_f, respectively. Finally

$$\boldsymbol{f} \triangleq \begin{bmatrix} v_r \\ \dfrac{v_t}{r} \\ -\dfrac{\mu_\odot}{r^2} + \dfrac{v_t^2}{r} + a_r \\ -\dfrac{v_r\, v_t}{r} + a_t \end{bmatrix} \tag{34}$$

is the vector that describes the spacecraft dynamics.

The optimal (i.e., minimum-time) trajectory has been obtained with an indirect approach by enforcing the necessary conditions for optimality according to the Pontryagin's maximum principle [58]. Given an optimal solution, there exists an absolutely continuous covector function $\boldsymbol{\lambda}$ and a covector $\boldsymbol{\nu}$ that satisfy the adjoint equations, the Hamiltonian maximization condition, the Hamiltonian value condition, the Hamiltonian evolution equation, and the transversality condition [58]. The Hamiltonian function H and the Endpoint Lagrangian $\bar{E}$ are given by

$$H = \boldsymbol{\lambda}^{\mathrm{T}} \boldsymbol{f}(\boldsymbol{x}(t),\, \alpha_t(t),\, \tau(t)) \quad , \quad \bar{E} = -t_f + \boldsymbol{\nu}^{\mathrm{T}} \boldsymbol{e}(\boldsymbol{x}(t_f)) \tag{35}$$

where the covector

$$\boldsymbol{\lambda} \triangleq \begin{bmatrix} \lambda_r & \lambda_\varphi & \lambda_{v_r} & \lambda_{v_t} \end{bmatrix}^{\mathrm{T}} \tag{36}$$

is the vector of the adjoint variables $\{\lambda_r,\, \lambda_\varphi,\, \lambda_{v_r},\, \lambda_{v_t}\}$ associated with the spacecraft states $\{r,\, \varphi,\, v_r,\, v_t\}$. The adjoint equations are

$$\dot{\boldsymbol{\lambda}} = -\frac{\partial H}{\partial \boldsymbol{x}} \tag{37}$$

from which it turns out that λ_φ is a constant of motion. According to the Pontryagin's maximum principle, the Hamiltonian maximization condition amounts to maximizing, at any time, the Hamiltonian function with respect to the control variables. If

$$\mathcal{H} \triangleq \max_{\alpha_t,\, \tau}(H) \tag{38}$$

the maximized Hamiltonian $\mathcal{H}$ is obtained by maximizing that portion of H (namely, H_c) that explicitly depends on the controls, or

$$H_c \triangleq \lambda_{v_r}\, a_r + \lambda_{v_t}\, a_t \tag{39}$$

The latter may also be rewritten as

$$H_c = \lambda_p\, (a_r \cos\alpha_\lambda + a_t \sin\alpha_\lambda) \tag{40}$$

where $\lambda_p \triangleq \sqrt{\lambda_{v_r}^2 + \lambda_{v_t}^2}$ is the magnitude of the primer vector $\boldsymbol{\lambda}_p \triangleq [\lambda_{v_r} \quad \lambda_{v_t}]^{\mathrm{T}}$ [64], while the primer vector angle $\alpha_\lambda \in [0,\, 2\pi)$ rad is defined such that

$$\cos\alpha_\lambda \triangleq \frac{\lambda_{v_r}}{\sqrt{\lambda_{v_r}^2 + \lambda_{v_t}^2}} \quad , \quad \sin\alpha_\lambda \triangleq \frac{\lambda_{v_t}}{\sqrt{\lambda_{v_r}^2 + \lambda_{v_t}^2}} \tag{41}$$

A comparison between Eqs. (29) and (40) demonstrates that the optimal control law is that shown in Fig. 8 by formally substituting α_d with α_λ. The Hamiltonian value condition provides the value of $\mathcal{H}$ at the final time t_f, given by

$$\mathcal{H}(\boldsymbol{\lambda}(t_f),\, \boldsymbol{x}(t_f)) = -\frac{\partial \bar{E}}{\partial t_f} \equiv 1 \tag{42}$$

Furthermore, the following Hamiltonian evolution equation holds

$$\frac{\mathrm{d}\mathcal{H}}{\mathrm{d}t} = \frac{\partial H}{\partial t} \equiv 0 \tag{43}$$

from which it turns out that the maximized Hamiltonian is a constant of motion. Bearing in mind Eq. (42), we obtain

$$\mathcal{H}(t) \equiv 1 \tag{44}$$

which plays a key role in the verification and validation of the computed numerical solution. Finally, the optimal solution satisfies the transversality condition, viz.

$$\boldsymbol{\lambda}(t_f) = \frac{\partial \bar{E}}{\partial \boldsymbol{x}(t_f)} \tag{45}$$

from which, using Eqs. (37), it is found that $\lambda_\varphi(t) \equiv 0$.

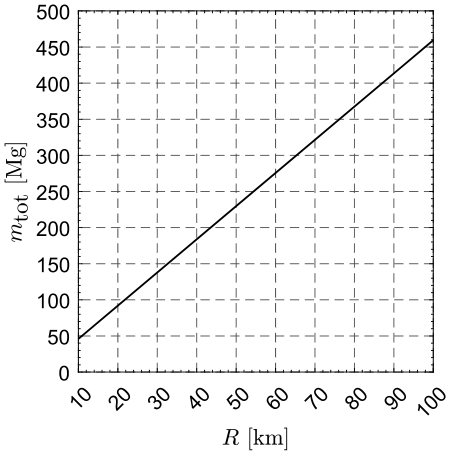

Fig. 10. Variation of m_{tot} with R when $f = 0.8$.

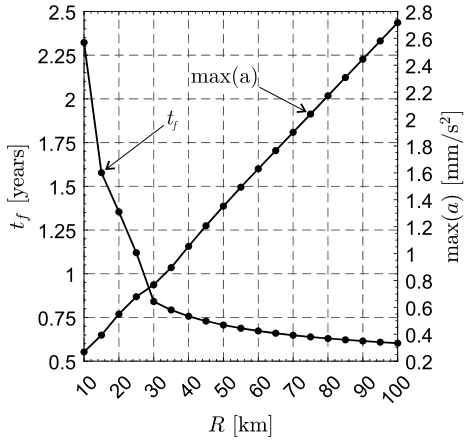

(a) Earth-Venus transfer.

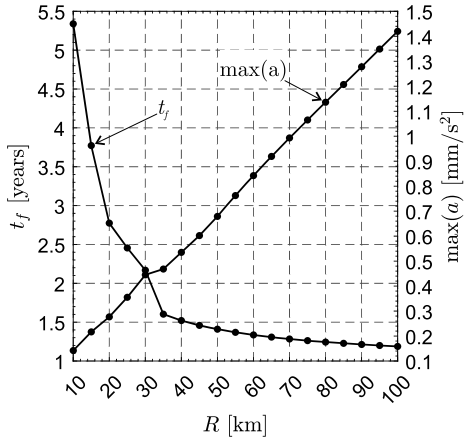

(b) Earth-Mars transfer.

Fig. 11. Variation of t_f and max(a) with R when $f = 0.8$.

6. Case study and numerical simulations

The proposed mathematical model is now used to analyze a set of minimum-time circle-to-circle interplanetary transfers. The spacecraft dynamics (31) has been integrated in double precision using a variable order Adams-Bashforth-Moulton solver scheme [65] with absolute and relative errors equal to 10^{-12}. For exemplary purposes, the SiLM parking orbit is assumed to be circular with radius $r_0 = r_\oplus \triangleq 1$ au. Such a choice describes the situation in which a SiLM leaves the sphere of influence of the Earth on a parabolic escape trajectory, with the simplifying assumption that the eccentricity of the Earth's heliocentric orbit is zero.

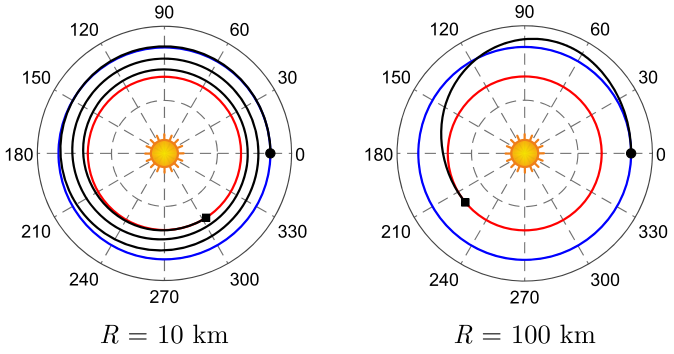

(a) Earth-Venus transfer.

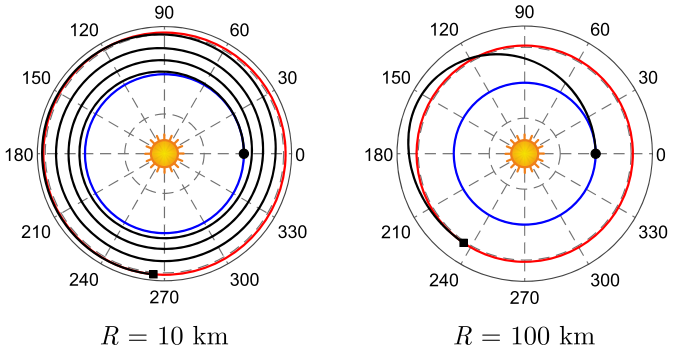

(b) Earth-Mars transfer.

Fig. 12. Transfer trajectories in the Earth-Venus and Earth-Mars scenarios when $f = 0.8$.

It is also assumed that the radius of the target orbit is $r_f = 0.723$ au (or $r_f = 1.524$ au), so that the simulations are consistent with an ephemeris-free Earth-Venus (or Earth-Mars) transfer, when the eccentricity and the mutual inclination between the planetary orbits are both neglected. Assuming that the SiLM system takes only 20% of the total spacecraft mass (i.e., $f = 0.8$), the minimum flight time t_f is sought by varying the sail radius within the interval $R \in [10, 100]$ km. In this case, the total mass changes with R as illustrated in Fig. 10.

Fig. 11 shows the obtained results for the two mission scenarios in terms of minimum flight time and maximum propulsive acceleration generated by the SiLM during the interplanetary transfer. In particular, Fig. 11(a) shows that t_f rapidly increases when $R < 30$ km, whereas Fig. 11(b) shows that this happens when $R < 35$ km. Finally, Fig. 12 shows the transfer trajectories related to the two cases when $R = 10$ km and $R = 100$ km, while Fig. 13 shows the corresponding optimal control parameters. Notably, $|\alpha_t^\star| \simeq 25$ deg in most of the transfer when $R = 10$ km (i.e., in case of a low-performance SiLM), while the optimal transfer trajectory is characterized by long coasting phases when $R = 100$ km (i.e., for a medium/high-performance SiLM). Finally note that the flight times may be further reduced if we considered a greater number of discrete data from the simulations; see Fig. 3. Nevertheless, the reduction in flight times can be expected to be not significant, especially for a low-performance SiLM, when the value of $|\alpha_t^\star|$ is the maximum admissible for most of the transfer.

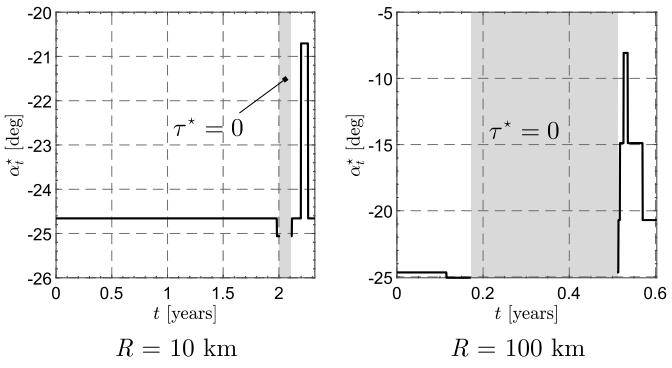

(a) Earth-Venus transfer.

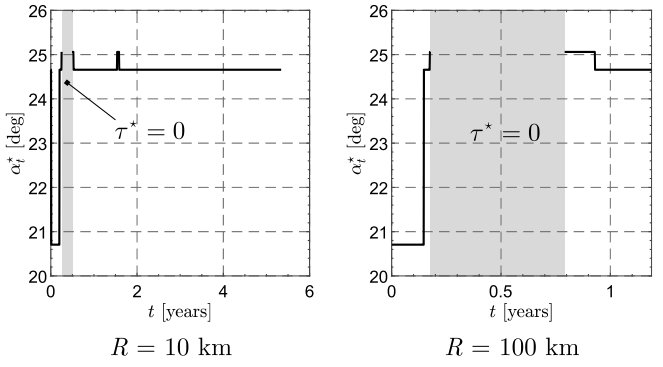

(b) Earth-Mars transfer.

Fig. 13. Optimal thrust angle $\alpha_t^\star$ and switching parameter $\tau^\star$ as a function of time in the Earth-Venus and Earth-Mars cases when $f = 0.8$.

7. Conclusions

This study has discussed an up-to-date mathematical model describing the propulsive acceleration vector provided by a single-loop MagSail and to exploit it in the analysis of minimum-time heliocentric transfer trajectories. A particle method has been initially chosen to evaluate the propulsive performance of a reference single-loop MagSail configuration. Then, the scaling relationships have been used to determine the single-loop MagSail performance as a function of suitable design parameters such as the coil radius. The proposed thrust model can be easily implemented in a simulation code for trajectory optimization and, in this sense, it represents an effective tool for preliminary mission analysis.

The resulting propulsive acceleration (related to the thrust through the total mass of the spacecraft) has been used in the analysis of minimum-time transfer trajectories between two circular heliocentric orbits using an indirect approach. The minimum flight times required to perform ephemeris-free Earth-Venus and Earth-Mars transfers have been calculated as a function of the coil radius by assuming a given value of the payload mass fraction. The numerical simulations have shown that the minimum flight time is less than one year when the coil radius is greater than 25 km in case of Earth-Venus transfers, and it is less than two years when the coil radius is greater than 30 km in case of Earth-Mars transfers.

Declaration of competing interest

The authors declare that they have no known competing financial interests or personal relationships that could have appeared to influence the work reported in this paper.

Data availability

The data that has been used is confidential.

References

[1] Z. Chi, F. Jiang, G. Tang, Optimization of variable-specific-impulse gravity-assist trajectories via optimality-preserving transformation, Aerosp. Sci. Technol. 101 (2020) 1–12, https://doi.org/10.1016/j.ast.2020.105828 (article no. 105828).

[2] Z. Yu, H. Shang, B. Wei, Accessibility assessment and trajectory design for multiple Near-Earth-asteroids exploration using stand-alone CubeSats, Aerosp. Sci. Technol. 118 (2021) 1–19, https://doi.org/10.1016/j.ast.2021.106944 (article no. 106944).

[3] A. Rubinsztejn, C.G. Sandel, R. Sood, F.E. Laipert, Designing trajectories resilient to missed thrust events using expected thrust fraction, Aerosp. Sci. Technol. 115 (2021) 1–12, https://doi.org/10.1016/j.ast.2021.106780 (article no. 106780).

[4] S. Firuzi, Y. Song, S. Gong, Gradient-index solar sail and its optimal orbital control, Aerosp. Sci. Technol. 119 (2021) 1–10, https://doi.org/10.1016/j.ast.2021.107103 (article no. 107103).

[5] A. Barles, M. Ceriotti, F. Ciampa, L. Felicetti, An optimal steering law for sailing with solar and planetary radiation pressure, Aerosp. Sci. Technol. 118 (2021) 1–13, https://doi.org/10.1016/j.ast.2021.107051 (article no. 107051).

[6] L. Niccolai, G. Mengali, A.A. Quarta, A. Caruso, Feedback control law of solar sail with variable surface reflectivity at Sun-Earth collinear equilibrium points, Aerosp. Sci. Technol. 106 (2020) 1–13, https://doi.org/10.1016/j.ast.2020.106144 (article no. 106144).

[7] C. Bianchi, L. Niccolai, L. Mengali, A.A. Quarta, Collinear artificial equilibrium point maintenance with a wrinkled solar sail, Aerosp. Sci. Technol. 119 (2021) 1–14, https://doi.org/10.1016/j.ast.2021.107150 (article no. 107150).

[8] W. Wang, A.A. Quarta, G. Mengali, J. Yuan, Multiple solar sail formation flying around heliocentric displaced orbit via consensus, Acta Astronaut. 154 (2019) 256–267, https://doi.org/10.1016/j.actaastro.2018.03.039.

[9] W. Wang, H. Baoyin, G. Mengali, A.A. Quarta, Solar sail cooperative formation flying around l_2-type artificial equilibrium points, Acta Astronaut. 169 (2020) 224–239, https://doi.org/10.1016/j.actaastro.2019.10.028.

[10] B. Fu, E. Sperber, F. Eke, Solar sail technology – A state of the art review, Prog. Aerosp. Sci. 86 (2016) 1–19, https://doi.org/10.1016/j.paerosci.2016.07.001.

[11] D.A. Spencer, L. Johnson, A.C. Long, Solar sailing technology challenges, Aerosp. Sci. Technol. 93 (2019) 1–12, https://doi.org/10.1016/j.ast.2019.07.009 (article no. 105276).

[12] M. Bassetto, A. Caruso, A.A. Quarta, G. Mengali, Optimal heliocentric transfers of a sun-facing heliogyro, Aerosp. Sci. Technol. 119 (2021) 1–14, https://doi.org/10.1016/j.ast.2021.107094 (article no. 107094).

[13] M. Bassetto, L. Niccolai, L. Boni, G. Mengali, A.A. Quarta, C. Circi, S. Pizzurro, M. Pizzarelli, R.C. Pellegrini, E. Cavallini, Sliding mode control for attitude maneuvers of Helianthus solar sail, Acta Astronaut. 198 (2022) 100–110, https://doi.org/10.1016/j.actaastro.2022.05.043.

[14] P. Janhunen, Electric sail for spacecraft propulsion, J. Propuls. Power 20 (2004) 763–764, https://doi.org/10.2514/1.8580.

[15] M. Bassetto, L. Niccolai, A.A. Quarta, G. Mengali, A comprehensive review of Electric Solar Wind Sail concept and its applications, Prog. Aerosp. Sci. 128 (2022) 1–27, https://doi.org/10.1016/j.paerosci.2021.100768 (article no. 100768).

[16] D.G. Andrews, R.M. Zubrin, Use of magnetic sails for Mars exploration missions, in: AIAA/ASME/SAE/ASEE 25th Joint Propulsion Conference, Monterey, US-CA, 1989, no. AIAA 89-2861.

[17] D.G. Andrews, R.M. Zubrin, Progress in magnetic sails, in: AIAA/ASME/SAE/ASEE 26th Joint Propulsion Conference, Orlando, FL, 16–18 July, 1990, paper AIAA 90-2367.

[18] D.G. Andrews, R.M. Zubrin, Magnetic sails and interstellar travel, J. Br. Interplanet. Soc. 43 (6) (1990) 265–272.

[19] R.M. Zubrin, D.G. Andrews, Magnetic sails and interplanetary travel, J. Spacecr. Rockets 28 (1991) 197–203, https://doi.org/10.2514/3.26230.

[20] R.M. Zubrin, The use of magnetic sails to escape from low Earth orbit, J. Br. Interplanet. Soc. 46 (3) (1992) 3–10, https://doi.org/10.2514/6.1991-3352.

[21] Y. Murayama, K. Ueno, Y. Oshio, H. Horisawa, I. Funaki, Preliminary results of magnetic field measurements on multi-coil magnetic sail in laboratory experiment, Vacuum 167 (2019) 509–513, https://doi.org/10.1016/j.vacuum.2018.05.004.

[22] K. Fujita, Particle simulation of moderately-sized magnetic sails, J. Space Technol. Sci. 20 (2) (2004) 26–31, https://doi.org/10.11230/jsts.20.2_26.

[23] D. Akita, K. Suzuki, Kinetic analysis on plasma flow of solar wind around magnetic sail, in: 36th AIAA Plasmadynamics and Lasers Conference, Toronto, Canada, 06–09 June, 2005, paper AIAA 2006-5227.

[24] H. Nishida, H. Ogawa, I. Funaki, K. Fujita, H. Yamakawa, Y. Inatani, Verification of momentum transfer process on magnetic sail using MHD model, in: 41st AIAA/ASME/SAE/ASEE Joint Propulsion Conference and Exhibit, Tucson, AZ, 10–13 July, 2005, paper AIAA 2005-4463.

[25] H. Nishida, H. Ogawa, I. Funaki, K. Fujita, H. Yamakawa, Y. Nakayama, Two-dimensional magnetohydrodynamic simulation of a magnetic sail, J. Spacecr. Rockets 43 (2006) 667–672, https://doi.org/10.2514/1.15717.
[26] T. Moritaka, H. Usui, M. Nunami, Y. Kajimura, M. Nakamura, M. Matsumoto, Full particle-in-cell simulation study on magnetic inflation around a magneto plasma sail, IEEE Trans. Plasma Sci. 38 (2010) 2219–2228, https://doi.org/10.1109/TPS.2010.2056392 (article no. 5551227).
[27] N. Yamamoto, M. Matsumoto, I. Funaki, Y. Yamagiwa, Magnetohydrodynamic numerical analysis of magnetic plasma sail including the effect of interplanetary magnetic field, in: 49th AIAA Aerospace Sciences Meeting Including the New Horizons Forum and Aerospace Exposition, Orlando, FL, 04–07 January, 2011, paper AIAA 2011-1073.
[28] Y. Kajimura, I. Funaki, M. Matsumoto, I. Shinohara, H. Usui, H. Yamakawa, Thrust and attitude evaluation of magnetic sail by three-dimensional hybrid particle-in-cell code, J. Propuls. Power 28 (2012) 652–663, https://doi.org/10.2514/1.B34334.
[29] Y. Ashida, I. Funaki, H. Yamakawa, Y. Kajimura, H. Kojima, Thrust evaluation of a magnetic sail by flux-tube model, J. Propuls. Power 28 (2012) 642–651, https://doi.org/10.2514/1.B34332.
[30] H. Nishida, I. Funaki, Analysis of thrust characteristics of a magnetic sail in magnetized solar wind, J. Propuls. Power 28 (2012) 636–641, https://doi.org/10.2514/1.B34260.
[31] I. Funaki, Y. Kajimura, Y. Ashida, H. Nishida, Y. Oshio, I. Shinohara, H. Yamakawa, The use of dipole plasma equilibrium for magnetic sail spacecraft, Fusion Sci. Technol. 63 (1T) (2013) 168–171, https://doi.org/10.13182/FST13-A16897.
[32] Y. Nagasaki, T. Nakamura, I. Funaki, Y. Ashida, H. Yamakawa, Conceptual design of YBCO coil with large magnetic moment for magnetic sail spacecraft, IEEE Trans. Appl. Supercond. 23 (2013) 1–5, https://doi.org/10.1109/TASC.2013.2243791 (article no. 6423254).
[33] Y. Ashida, H. Yamakawa, I. Funaki, H. Usui, Y. Kajimura, H. Kojima, Thrust evaluation of small-scale magnetic sail spacecraft by three-dimensional particle-in-cell simulation, J. Propuls. Power 30 (2014) 186–196, https://doi.org/10.2514/1.B35026.
[34] Y. Ashida, I. Funaki, H. Yamakawa, H. Usui, Y. Kajimura, H. Kojima, Two-dimensional particle-in-cell simulation of magnetic sails, J. Propuls. Power 30 (2014) 233–245, https://doi.org/10.2514/1.B34692.
[35] C. Gros, Universal scaling relation for magnetic sails: momentum braking in the limit of dilute interstellar media, J. Phys. Commun. 1 (2017) 1–11, https://doi.org/10.1088/2399-6528/aa927e (article no. 045007).
[36] H. Kojima, I. Funaki, Y. Shimizu, H. Yamakawa, S. Shinohara, Y. Nakayama, Experimental simulation of a plasma flow around magnetic sail, in: 29th International Electric Propulsion Conference, Princeton, NJ, October 31–November 4, 2005, paper IEPC-2005-107.
[37] I. Funaki, H. Yamakawa, Y. Shimizu, Y. Nakayama, H. Horisawa, K. Ueno, T. Kimura, Experimental simulation of magnetic sails, in: 42nd AIAA/ASME/SAE/ASEE Joint Propulsion Conference and Exhibit, Sacramento, CA, 09–12 July, 2006, paper AIAA 2006-5227.
[38] I. Funaki, H. Kojima, H. Yamakawa, Y. Nakayama, Y. Shimizu, Laboratory experiment of plasma flow around magnetic sail, Astrophys. Space Sci. 307 (1–3) (2007) 63–68, https://doi.org/10.1007/s10509-006-9251-4.
[39] I. Funaki, K. Ueno, H. Yamakawa, Y. Nakayama, T. Kimura, H. Horisawa, Interaction between plasma flow and magnetic field in scale model experiment of magnetic sail, Fusion Sci. Technol. 51 (2T) (2007) 226–228, https://doi.org/10.13182/fst07-a1357.
[40] K. Ueno, I. Funaki, T. Kimura, H. Horisawa, H. Yamakawa, Thrust measurement of a pure magnetic sail using parallelogram-pendulum method, J. Propuls. Power 25 (2009) 536–539, https://doi.org/10.2514/1.39211.
[41] Y. Kajimura, H. Usui, I. Funaki, K. Ueno, M. Nunami, I. Shinohara, M. Nakamura, H. Yamakawa, Hybrid particle-in-cell simulations of magnetic sail in laboratory experiment, J. Propuls. Power 26 (2010) 159–166, https://doi.org/10.2514/1.45096.
[42] Y. Oshio, I. Funaki, K. Ueno, The dynamic behavior of magnetic sails in laboratory, in: 47th AIAA/ASME/SAE/ASEE Joint Propulsion Conference and Exhibit, San Diego, CA, 31 July–03 August, 2011, paper AIAA 2011-5998.
[43] Y. Nagasaki, T. Nakamura, I. Funaki, Y. Ashida, H. Yamakawa, Coupled-analysis of current transport performance and thermal behaviour of conduction-cooled Bi-2223/Ag double-pancake coil for magnetic sail spacecraft, Phys. C Supercond. Appl. 492 (2013) 96–102, https://doi.org/10.1016/j.physc.2013.06.004.
[44] N. Shah, Lunar Magsail - Conceptual magnetic sail design for lunar missions, in: 31st Joint Propulsion Conference and Exhibit, San Diego, CA, 10–12 July, 1995, paper AIAA 95-2370.
[45] S.G. Love, D.G. Andrews, Applications of magnetic sails, Acta Astronaut. 26 (8–10) (1992) 643–651, https://doi.org/10.1016/0094-5765(92)90154-B.
[46] D.G. Andrews, Interstellar propulsion opportunities using near-term technologies, Acta Astronaut. 55 (3–9) (2004) 443–451, https://doi.org/10.1016/j.actaastro.2004.05.038.
[47] A.A. Quarta, G. Mengali, G. Aliasi, Optimal control laws for heliocentric transfers with a magnetic sail, Acta Astronaut. 89 (2013) 216–225, https://doi.org/10.1016/j.actaastro.2013.04.018.
[48] M. Bassetto, A.A. Quarta, G. Mengali, Magnetic sail-based displaced non- Keplerian orbits, Aerosp. Sci. Technol. 92 (2019) 363–372, https://doi.org/10.1016/j.ast.2019.06.018.
[49] M. Bassetto, A.A. Quarta, G. Mengali, Generalized sail trajectory approximation with applications to MagSails, Aerosp. Sci. Technol. 118 (2021) 1–9, https://doi.org/10.1016/j.ast.2021.106991 (article no. 106991).
[50] N. Perakis, A.M. Hein, Combining magnetic and electric sails for interstellar deceleration, Acta Astronaut. 128 (2016) 13–20, https://doi.org/10.1016/j.actaastro.2016.07.005.
[51] H. Ren, T. Yuan, M. Huo, C. Zhao, S. Zeng, Dynamics and control of a full-scale flexible electric solar wind sail spacecraft, Aerosp. Sci. Technol. 119 (2021) 1–22, https://doi.org/10.1016/j.ast.2021.107087 (article no. 107087).
[52] W. Wang, G. Mengali, A.A. Quarta, H. Baoyin, Decentralized fault-tolerant control for multiple electric sail relative motion at artificial lagrange points, Aerosp. Sci. Technol. 103 (2020) 1–12, https://doi.org/10.1016/j.ast.2020.105904 (article no. 105904).
[53] X. Pan, A.A. Quarta, G. Mengali, M. Xu, Linearized relative motion and proximity control of e-sail-based displaced orbits, Aerosp. Sci. Technol. 99 (2020) 1–9, https://doi.org/10.1016/j.ast.2019.105574 (article no. 105574).
[54] N. Perakis, Maneuvering through solar wind using magnetic sails, Acta Astronaut. 177 (2020) 122–132, https://doi.org/10.1016/j.actaastro.2020.07.029.
[55] A. Peloni, A.V. Rao, M. Ceriotti, Automated trajectory optimizer for solar sailing (ATOSS), Aerosp. Sci. Technol. 72 (2018) 465–475, https://doi.org/10.1016/j.ast.2017.11.025.
[56] Y. Song, S. Gong, Solar-sail trajectory design for multiple near-Earth asteroid exploration based on deep neural networks, Aerosp. Sci. Technol. 91 (2019) 28–40, https://doi.org/10.1016/j.ast.2019.04.056.
[57] A.E. Bryson, Y.C. Ho, Applied Optimal Control, Hemisphere Publishing Corporation, New York, NY, ISBN 0-891-16228-3, 1975, pp. 71–89, Ch. 2.
[58] I.M. Ross, A Primer on Pontryagin's Principle in Optimal Control, Collegiate Publishers, ISBN 9780984357116, 2015, pp. 127–129, Ch. 2.
[59] D. Wu, W. Wang, F. Jiang, J. Li, Minimum-time low-thrust many-revolution geocentric trajectories with analytical costates initialization, Aerosp. Sci. Technol. 119 (2021), https://doi.org/10.1016/j.ast.2021.107146 (article no. 107146).
[60] M. Raible, Concept development for a magnetic sail deceleration system, Ph.D. thesis, Technical, University of Munich, 2013.
[61] P. Chaddah, Critical current densities in superconducting materials, Sadhana. Acad. Proc. Eng. Sci. 28 (1–2) (2003) 273–282, https://doi.org/10.1007/BF02717137.
[62] M. LeRoux, K.J. Kihlstrom, S. Holleis, M.W. Rupich, S. Sathyamurthy, S. Fleshler, H.P. Sheng, D.J. Miller, S. Eley, L. Civale, A. Kayani, P.M. Niraula, U. Welp, W.-K. Kwok, Rapid doubling of the critical current of Y $Ba_2Cu_3O_{7-\delta}$ coated conductors for viable high-speed industrial processing, Appl. Phys. Lett. 107 (2015) 1–6, https://doi.org/10.1063/1.4935335 (article no. 192601).
[63] R. Xie, A.G. Dempster, An on-line deep learning framework for low-thrust trajectory optimisation, Aerosp. Sci. Technol. 118 (2021) 1–15, https://doi.org/10.1016/j.ast.2021.107002 (article no. 107002).
[64] D.F. Lawden, Optimal Trajectories for Space Navigation, Butterworths & Co., London, 1963, pp. 54–60.
[65] L.F. Shampine, M.W. Reichelt, The MATLAB ODE suite, SIAM J. Sci. Comput. 18 (1) (1997) 1–22, https://doi.org/10.1137/S1064827594276424.